


Article

# Effects of V and Cr on Laser Cladded Fe-Based Coatings

Haiyang Wang <sup>1</sup>, Song Zhang <sup>1,\*</sup> , Chunhua Zhang <sup>1</sup>, Chenliang Wu <sup>1</sup>, Jingbo Zhang <sup>2</sup> and Adil O. Abdullah <sup>3</sup> 

<sup>1</sup> School of Materials Science and Engineering, Shenyang University of Technology, Shenyang 110870, China; marine\_why@163.com (H.W.); zhangch5858@126.com (C.Z.); mfclwu@163.com (C.W.);

<sup>2</sup> Shenyang Dalu Laser Technology CO., Ltd., Shenyang 110136, China; daluzhangjingbo@163.com

<sup>3</sup> School of Stomatology, China Medical University, Shenyang 110002, China; adilabdullah@cmu.edu.cn

\* Correspondence: songzhang\_sy@163.com (S.Z.); Tel.: +86-242-549-4578

Received: 7 February 2018; Accepted: 13 March 2018; Published: 15 March 2018

**Abstract:** Fe-based coatings with high V and Cr content were obtained by laser cladding using Fe-based powder with different Cr<sub>3</sub>C<sub>2</sub> and FeV<sub>50</sub> content. The results showed that Fe-based coatings were uniform and dense. The constituent phases were mainly composed of α-Fe solid solution with the increase of Cr<sub>3</sub>C<sub>2</sub> and FeV<sub>50</sub>, γ-Fe and V<sub>8</sub>C<sub>7</sub> phases were achieved. The microstructure of the coatings exhibited a typical dendrite structure. The concentration of C, V and Cr were saturated in dendritic areas, and the other alloying elements were mainly dissolved in the interdendritic areas. The hardness and wear resistance of Fe-based coatings were enhanced with the Cr<sub>3</sub>C<sub>2</sub> and FeV<sub>50</sub> addition. The specimen with 15% Cr<sub>3</sub>C<sub>2</sub> and 16% FeV<sub>50</sub> had the highest hardness of 66.1 ± 0.6 HRC, which was 1.05 times higher than the sample with 4.5% Cr<sub>3</sub>C<sub>2</sub> and 5% FeV<sub>50</sub>, and the wear resistance of the former was three times greater than the latter.

**Keywords:** laser cladding; Fe-based coating; microstructure; hardness; wear resistance

## 1. Introduction

Recently, the diesel engine is getting smaller, and the service environment of the internal components has also increased rapidly due to the requirement of the energy conservation and emission reduction [1]. Traditional carburizing and the quenching process have been unable to meet the requirements of modern production for diesel engine camshaft because of the camshaft, as the main component of the engine transmission system, usually made of low alloy steel or cast iron, suffers from an increasing load. Within a shorter period, adhesive wear or other failure modes may occur on the surface of the camshaft, which will cause the decrease of service life [2]. Consequently, enhancing the surface wear resistance of the camshaft is an effective solution to improving service life.

Laser cladding, as an advanced laser surface engineering, has been studied by many researchers [3–6] and been utilized in various commercial applications [7–11]. Laser cladding technology uses a high energy laser beam to melt metal powder materials, and a high performance thick coating with a metallurgical joint to the substrate can be obtained directly with a small amount of subsequent processing [12]. Compared with the other coating technologies, laser cladding has various advantages, such as realizing a highly refined microstructure, low dilution ratio and limited heat affected zone [13]. Meanwhile, laser cladding technology also has the advantages of accurate control and small deformation. The preparation of high performance coating on the surface of low-cost materials by laser cladding technology can save a great deal of precious metals, which significantly alleviates the issue of energy, resources and has a good prospect of engineering application [14]. Thus, this laser cladding process has the potential to replace the traditional carburizing and quenching process to produce camshafts with higher wear resistance.

Fe-based alloy powder has certain advantages such as the wide range of sources, low price, and closing to the composition of the substrate and acceptable compatibility [15]. To meet the different requirements under certain circumstances, alloying elements, such as vanadium, titanium, niobium and chromium, are added into Fe-based powder to manufacture different parts with diverse properties. Adding a small amount of vanadium into steel makes the steel more resilient, stronger, and has a better wear and crack resistance [16]. The Cr element improved not only the corrosion resistance by improving the electrode potential of Fe-based alloy and forming a passivation film on the alloy surface [17–19], but also the mechanical properties such as high-temperature strength, hardness and wear resistance [20–22]. Due to the outstanding property of the vanadium and chromium, certain investigators started to study the impact of the vanadium and the chromium on the Fe-based alloys. Ke et al. [23] have investigated the influence of Nb/V content between 0 and 6% on Mo<sub>2</sub>FeB<sub>2</sub> ceramic-steel produced by liquid phase reaction sintering, the results revealed that the hardness and transverse rupture strength both enhance first and then descends. Mo<sub>2</sub>FeB<sub>2</sub> ceramic-steel with 4 wt % and 2 wt % V show the best hardness and transverse rupture strength. Kanalec and Górný [24] have investigated the influence of VC morphology on the mechanical properties for Fe-C-V casting alloys. The results proved that the spheroidising treatment of VC carbides increases the tensile strength by 60%, elongation 14–21 times, and the wear resistance more than twice as high as the abrasion-resistance cast steel. Gwon et al. [25] have investigated the effect of the V addition (0.1 wt %–0.3 wt %) on the microstructure and the tensile behavior of hot rolling TWIP steel. The results have shown that the V additions contributed to a reduction in the grain size and an increase in the yield strength of the TWIP steels. Effects of different addition of Cr on TiC–VC reinforced Fe-based laser cladding coatings were also investigated by Zhang et al. [26]. The study revealed that the TiC–VC reinforced Fe-based laser cladding coatings with different addition of Cr were composed of  $\alpha$ -Fe,  $\gamma$ -Fe, TiC, VC and TiVC<sub>2</sub>, the cladding layer with 3.0% Cr showed the highest microhardness 1090HV<sub>0.2</sub> and the cladding layer with 12.0% Cr addition showed the best corrosion resistance. The reported literature shows that the influence of vanadium and chromium on the properties of Fe-based alloys produced by different technologies such as casting, hot rolling and sintering, etc. was investigated in detail. However, the study on the impact of the high content of Cr and V on laser clad coating was rarely reported.

In the present study, three Fe-based coatings with high V and Cr content on 35CrMo steel by laser cladding using Fe-based powder with different Cr<sub>3</sub>C<sub>2</sub> and FeV<sub>50</sub> content were achieved. The constituent phases, microstructure, hardness and wear resistance of the coatings were investigated.

## 2. Materials and Methods

Homemade stainless steel powder with the nominal composition in wt %:  $\leq 0.18$  C; 15.5–17.5 Cr; 1.60–1.80 Ni; 1.05–1.25 Si; 1.00 Mo;  $\leq 0.50$  Mn; 1.15–1.35 B; and balance Fe, commercially available Cr<sub>3</sub>C<sub>2</sub> powder and FeV<sub>50</sub> powder were used as feedstock materials. FeV<sub>50</sub> powder was used as the source of vanadium in the coating as the chemical composition is shown in Table 1. Three different powders were achieved by adjusting the proportion of stainless steel, Cr<sub>3</sub>C<sub>2</sub> and FeV<sub>50</sub> powders, as shown in Table 2. Prior to laser cladding, the powder mixture was meticulously mixed with the aid of a ball milling equipment in an argon atmosphere for 1 h, and then dried in a furnace at 80 °C for 8 h. The 35CrMo plain roll steel, as a kind of low alloy steel used in the environment suffered impact, bending-torsion and high load, was used as the substrate with a size of  $\Phi 150$  mm  $\times$  15 mm and nominal composition in wt %: 0.32–0.40 C, 0.17–0.37 Si, 0.40–0.70 Mn, 0.8–1.1 Cr, 0.15–0.25 Mo, and balance Fe. The substrate was well treated by grinding with 600 SiC paper and cleaning with acetone. The laser clad Fe-based coatings were manufactured using an Ytterbium Laser System (YLS-6000, IPG Photonics, Beijing, China) with a wavelength of 1070 nm and maximum output power of 6 kW. After a series of trial runs, the optimized process parameters were obtained: laser power 3500 W, beam scanning speed 300 mm/min, powder feed rate 18 g/min, shielding gas (Ar) 400–500 L/h, laser beam diameter 4 mm and overlapping rate 30%.

The coating samples were cross-sectioned perpendicular to the laser scanning direction with electrical discharge wire cutting, followed by conventional metallography preparation procedures. Then, the samples were etched with an aqueous solution consisted of 45 mL HCl + 15 mL HNO<sub>3</sub> + 60 mL distilled water. The microstructure of coatings was observed using scanning electron microscopy (SEM, S-3400, Hitachi, Tokyo, Japan) coupled with an energy dispersive spectrometer (EDS, S-3400N, Hitachi, Yokohama, Japan). The constituent phases of the coatings were identified by an X-ray diffraction (XRD, Shimadzu 7000, Shimadzu, Kyoto, Japan) in the 2 $\theta$  range of 20° to 100°, using Cu K $\alpha$  radiation at 40 kV and 30 mA with a speed of 4°/min. The hardness was measured with an HR-150A rockwell hardness tester (HR-150A, Lai Hua Ltd., Laizhou, China) under 150 kg load for 10 s. Coating samples for reciprocating wear test were cut from the laser cladding specimens as cuboids with the size of 10 mm  $\times$  10 mm  $\times$  15 mm, and ground clean with SiC paper and polished with 2.5 mm diamond paste in order to obtain identical surface roughness. Reciprocating wear tests were carried out with a MFT-4000 multi-function experimental apparatus (Lanzhou Huahui Instrument Technology Co., Ltd., Lanzhou, China) of material surface properties in the ball-on-plate configuration. A Si<sub>3</sub>N<sub>4</sub> ball of diameter 5 mm was used in the test, with a stroke length of 7 mm, a normal load of 10 N, a sliding velocity of 120 mm/min and a duration of 60 min. The profiles across the wear tracks and the wear volume were measured using a surface profilometer (Micro XAM-3D, KLA-Tencor Corporation, Shanghai, China). The product of the cross-section area and the stroke length was used to act as wear volume.

**Table 1.** Chemical composition of FeV<sub>50</sub>.

Elements	Content [wt %]
V	50
C	< 0.4
Si	< 2.0
P	< 0.06
S	< 0.04
Al	< 1.5
Fe	Bal.

**Table 2.** Powder proportion of the laser cladded Fe-based coating powders (wt %).

Cladding Powders	Stainless Steel	Cr <sub>3</sub> C <sub>2</sub>	FeV <sub>50</sub>
S1	90.5	4.5	5
S2	74.5	7.5	8
S3	69	15	16

### 3. Results and Analysis

#### 3.1. Microstructure

Figure 1 shows the cross section of the laser cladded Fe-based coatings at low magnification. It is obvious from Figure 1 that the laser cladded Fe-based coatings were dense and uniform with no holes, cracks or other defects. The average thickness of the laser cladded Fe-based coatings is 1440  $\mu$ m, 1440  $\mu$ m and 1600  $\mu$ m, respectively, indicating that the elements of V and Cr rarely have influence on the thickness. Figure 2 shows the cross-sectional SEM view of Fe-based alloy coatings. The interfaces of the laser cladded coatings are shown in Figure 2a–c. It is clear that the microstructure of the three coatings presented a typical dendrite structure growing from the substrate. The microstructure near the interface of S1 and S2 was mainly composed of columnar dendrite phase, which of S3 was cellular dendrite. A layer of planar crystallization with a thickness of about 5  $\mu$ m was found near the interfaces of the laser cladded layers, indicating that a good metallurgical bonding between the coating and the substrate was achieved. The microstructure in middle sections of laser cladded coatings is

shown in Figure 2d–f. The coatings exhibited dendrites (area DR) and interdendritic region (area ID) microstructure. Using the quantitative metallographic method as reported elsewhere [27], the area fraction of dendrites in the area was measured with a result of 91.50%, 89.06% and 84.38%, indicating that the grain size decreased with the addition of Cr<sub>3</sub>C<sub>2</sub> and FeV<sub>50</sub>. To figure out the distribution of alloy elements, EDS analysis was carried out as shown in Figure 1. It can be seen that the contents of main elements C, V and Cr in dendrites (area DR) were similar and were not varied with the addition of the Cr<sub>3</sub>C<sub>2</sub> and the FeV<sub>50</sub>, indicating that C, V and Cr were almost saturated. However, the contents of C, V and Cr in the interdendritic region (area ID) presented a trend of increase with the increase of Cr<sub>3</sub>C<sub>2</sub> and FeV<sub>50</sub> content.

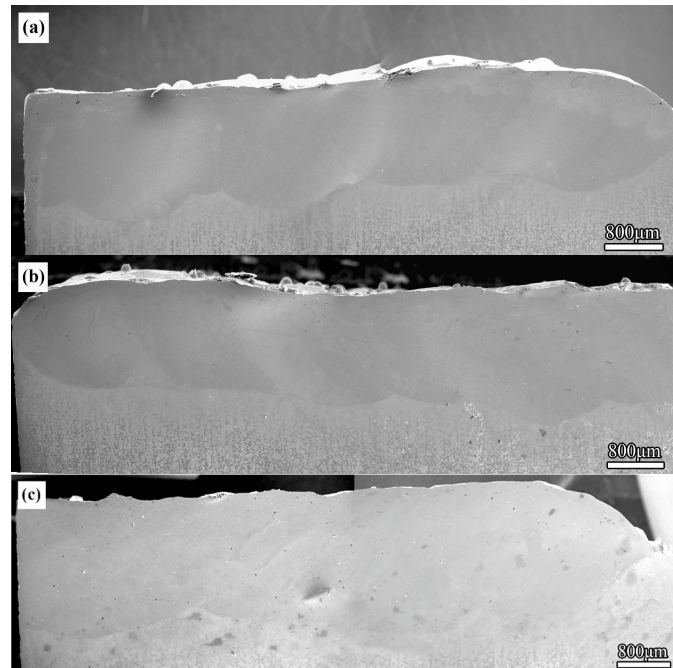


Figure 1. Cross section of the laser cladded Fe-based coatings at low magnification (a) S1; (b) S2; (c) S3.

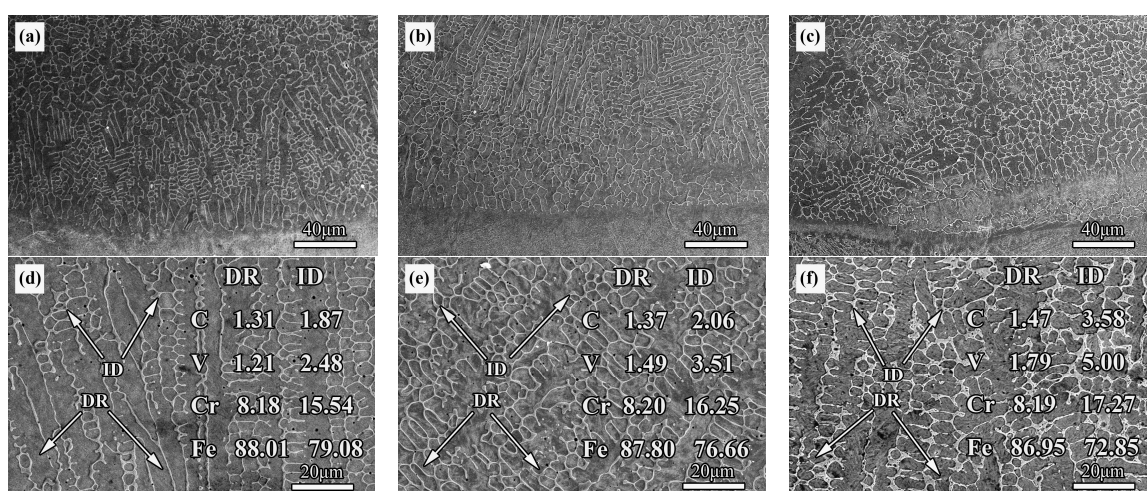


Figure 2. SEM images of the interface and the microstructures of the laser cladded Fe-based coatings: (a,d) S1; (b,e) S2; (c,f) S3.

According to the theory of metal solidification [28], the undercooling  $\Delta T$  caused by concentration gradient is extremely higher than that caused by heat flow and interface curvature. The  $\Delta T$  in the front of columnar crystal could be expressed as:

$$\Delta T = \Delta T_c = (\alpha V)^{\frac{1}{n}} \quad (1)$$

where  $\alpha$  and  $n$  are the constants related to the alloy, and  $V$  is the cooling rate. The liquid temperature gradient  $G_L$  could be expressed as [29]:

$$G_L = \frac{1}{n+1} \sqrt[3]{\frac{-4\pi}{3 \ln(1-\phi)}} \left(1 - \frac{\Delta T_n^{n+1}}{\Delta T^{n+1}}\right) \Delta T N_0^{1/3} \quad (2)$$

where  $\phi$ ,  $\Delta T_n$  and  $N_0$  stand for the volume fraction of equiaxed grain, the nucleation undercooling, and the density of nucleation sites, respectively. The cooling rate during laser cladding process was high, which indicated a high undercooling  $\Delta T$ , hence the nucleation undercooling  $\Delta T_n$  could be neglected in this study. Combining with the formulas (1) and (2), the liquid temperature gradient  $G_L'$  in laser cladding process could be given by:

$$(G_L)^n = \alpha V \left[ \frac{1}{n+1} \sqrt[3]{\frac{-4\pi N_0}{3 \ln(1-\phi)}} \right]^n \quad (3)$$

It is important to note that the liquid temperature gradient  $G_L'$  of cladding metal increased with increasing cooling rate. According to the earlier argument, the followed measures could be taken to inhibit the growth of dendrites: (1) decreasing the scanning speed of laser to reduce the cooling rate, which decreased the  $G_L'$  of cladding metal; (2) preheating the substrate to decrease the  $G_L'$  of cladding metal; and (3) increasing the density of nucleation sites  $N_0$  to raise the critical temperature gradient. The content of FeV<sub>50</sub> increased gradually while compared with the composition of cladding powders as shown in Table 2. The FeV<sub>50</sub> in the feedstock materials was heated and decomposed into Fe and V elements during the laser cladding process, which increased the V content in the molten pool. The decomposed V element acted as nucleating agents in Fe-based alloy to increase the density of nucleation sites  $N_0$  and prevent the growth of dendrites. Furthermore, large amounts of C, V and Cr dissociated into the interdendritic regions, which reduced disorder and the internal energy of the interdendritic region. Consequently, it is extremely difficult for interdendritic regions to slip; therefore, the mobility of the interdendritic regions decreased. This causes the decrease of grain size and refinement of the microstructure by the solute drag effect [30].

### 3.2. Constituent Phase

Figure 3 shows the XRD spectra of Fe-based alloy coatings. It is obviously observed that the S1 and S2 were composed of  $\alpha$ -Fe solid solution and Cr<sub>23</sub>C<sub>6</sub> phase. With the increase of Cr<sub>3</sub>C<sub>2</sub> and FeV<sub>50</sub>, the diffraction peaks of  $\gamma$ -Fe and V<sub>8</sub>C<sub>7</sub> also appeared besides the  $\alpha$ -Fe solid solution in the XRD spectrum of S3. In addition, the content of C, V and Cr elements increased with the addition of Cr<sub>3</sub>C<sub>2</sub> and FeV<sub>50</sub> in ID; therefore, it is reasonable to deduce that V<sub>8</sub>C<sub>7</sub> and Cr<sub>23</sub>C<sub>6</sub> existed in the ID region of S3. The presence of  $\gamma$ -Fe in S3 can be explained as: (a) the diffusion velocity of V and Cr elements in ferrite was slower than other phases such as austenite and martensite, so that the diffusion of C element was hindered by the high content of V and Cr, which resulted in the formation of the carbon-rich areas (b) due to the rapid melting and solidification through the laser cladding process, and the molten pool could not homogenize before solidified completely. A mass of C elements generated by decomposition of Cr<sub>3</sub>C<sub>2</sub> gathered in a carbon-rich area. The Ms (martensite transformation temperature) points of martensite in these areas were reduced where the austenite showed a higher stability [31]. In addition, as shown in Table 3, the diffraction angle ( $2\theta$ ) of  $\alpha$ -Fe decreased and the  $2\theta$  displacement increased

with the addition of  $\text{Cr}_3\text{C}_2$  and  $\text{FeV}_{50}$ , which indicated that the lattice distortion in  $\alpha$ -Fe solid solution was increased.

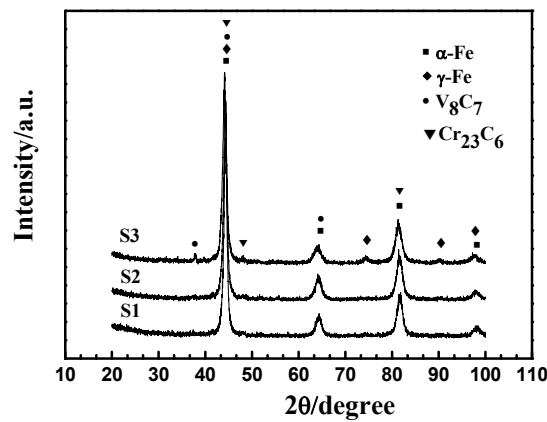


Figure 3. X-ray diffraction spectra of the laser cladded Fe-based coatings.

Table 3. XRD data showing variation in diffraction angle of  $\alpha$ -Fe and  $2\theta$  displacement.

Coating Sample	Diffraction Angle ( $^{\circ}$ )	$2\theta$ Displacement ( $^{\circ}$ )
Standard diffraction angle	44.67	0
S1	44.32	0.35
S2	44.26	0.41
S3	44.16	0.51

### 3.3. Hardnes

Figure 4 shows the hardness of the Fe-based alloy coatings. It made evident that the average hardness of coating samples increased with the addition of  $\text{Cr}_3\text{C}_2$  and  $\text{FeV}_{50}$ . The average hardness for S1, S2 and S3 was  $62.9 \pm 0.6$  HRC,  $65.3 \pm 0.5$  HRC and  $66.1 \pm 0.6$  HRC, respectively. In addition, the hardness achieved in coatings prepared by laser cladding in the current study was much higher than the other similar coatings, which was reported in different literature. It has reported a microhardness of 650 HV for H13 tool steel laser coating and 659 HV for AISI 420 martensitic stainless steel laser coating [32]. The high hardness was mainly attributed to the high solid solubility of C, V and Cr elements. The rapid solidification of the laser cladding process led to an extension of the solubility limit [33]. Increasing C, V and Cr atoms increase lattice distortion and improve the effect of solid solution strengthening, which was consistent with the XRD results [34]. The differences among the average hardness of the three laser-cladded coatings were related to the disparities of grain size caused by the different content of V and Cr [35]. The improvement of yield strength could be quantified by the classic Hall–Petch equation below [36]:

$$\sigma_i = \sigma_0 + Kd^{-1/2} \quad (4)$$

where  $\sigma_i$ ,  $\sigma_0$ ,  $K$ , and  $d$  stand for the tensile or yield strength, a constant stress for steel material, the Hall–Petch slope, and the mean grain size of steel material, respectively. The proportional relation indicated that the tensile or yield strength value positively correlated to the reciprocal root of the grain size. The strength value increased with the decrease of the grain size. The influence of grain size on strength was found to be identical to that on material hardness [37]. Otherwise, the formation of the  $\text{V}_8\text{C}_7$  was also an important factor to increase the hardness. The nucleation of the second phase of  $\text{V}_8\text{C}_7$  may take place first, and the crystal nucleus provided a place for heterogeneous nucleation, which increased the number of grains and decreased the grain size. Hence, this increases the amount of grain boundaries, and generates the so-called grain boundary strengthening [38].

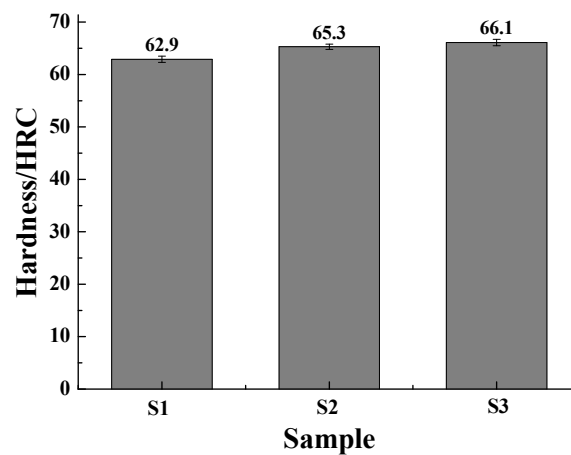


Figure 4. Hardness of the laser clad Fe-based coatings.

### 3.4. Wear Resistance

The wear resistance was measured by specific wear rate, which is defined as [39]:

$$\text{Specific wear rate} = V/(FL) \quad (5)$$

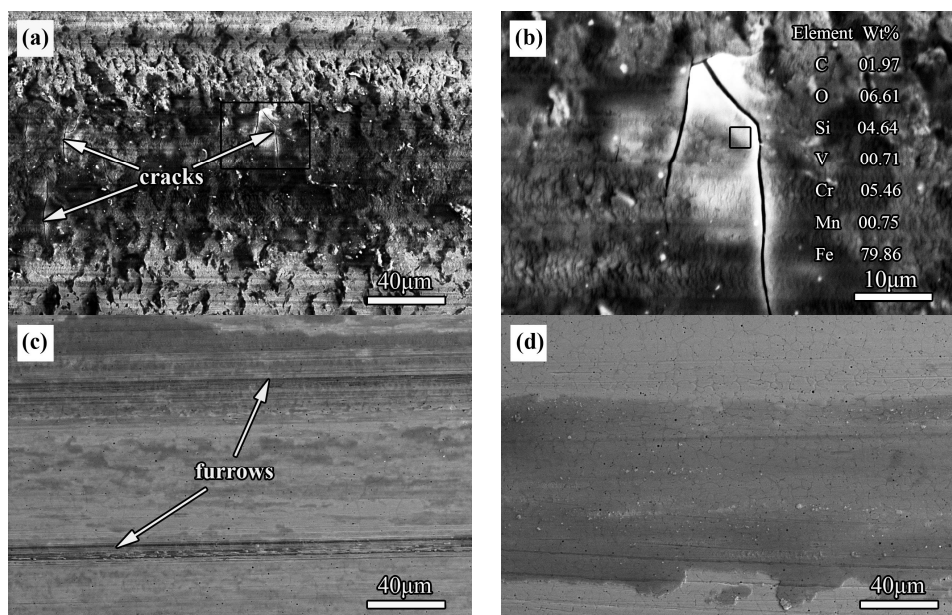
where  $V$ ,  $F$ , and  $L$  stand for the volumetric loss of the sample, the normal load, and the sliding distance, respectively. The wear volume and specific wear rate of laser clad coatings were listed in Table 4. Higher wear resistance was corresponding to smaller specific wear rate as lower volume was removed after sliding the same distance at the similar normal load. It can be easily observed that the wear resistance showed a trend of increasing with the addition of  $\text{Cr}_3\text{C}_2$  and  $\text{FeV}_{50}$ . The specific wear rate of S1 was the highest one roughly about  $8.66 \times 10^{-8} \text{ mm}^3 \text{ N}^{-1} \text{ m}^{-1}$ , while the specific wear rate of S3 was the lowest about  $2.80 \times 10^{-8} \text{ mm}^3 \text{ N}^{-1} \text{ m}^{-1}$ . The specific wear rate of S1 and S2 was 3 and 1.8 times larger than the S3. Combined with the results of average hardness, it can be observed that the highest wear resistance of S3 corresponded to the highest hardness, which is consistent with Archard's law. Moreover, the specific wear rate of the laser cladding Fe-based coatings are much lower than that of the TiC/Fe cermet electrical discharge coating [40] and as-annealed DPD 316L SS samples [41] with the specific wear rate of  $\sim 10.0 \times 10^{-6} \text{ mm}^3 \text{ N}^{-1} \text{ m}^{-1}$  and  $3.26 \times 10^{-6} \text{ mm}^3 \text{ N}^{-1} \text{ m}^{-1}$ , respectively.

Table 4. Wear volumes and specific wear rates of coatings in a reciprocating wear condition.

Specimen	Wear Volume ( $\mu\text{m}^3$ )	Specific Wear Rate ( $\text{mm}^3/\text{N m}$ )
S1	$6.238 \times 10^6$	$8.66 \times 10^{-8}$
S2	$3.639 \times 10^6$	$5.05 \times 10^{-8}$
S3	$2.013 \times 10^6$	$2.80 \times 10^{-8}$

To illustrate the wear mechanisms of the coatings, the worn surfaces are characterized by SEM as shown in Figure 5. It can be clearly seen that the worn surface of S1 was characterized by vestiges of material spalling and plastic deformation (see Figure 5a). In addition, cracks vertical to the worn scar were observed. During sliding, the cracks may spread when they were subjected to the combined effect of normal force and tangential force, leading to material spalling. The EDS analysis was taken on the surface of worn scars. The results indicated that the worn surface contained high levels of oxygen (see Figure 5b), indicating that oxidation occurred on the worn surface. The oxide debris may adhere to the worn surface, which caused abrasive wear during reciprocating wear. This indicated that the wear mechanism of S1 was composed of abrasive, adhesive and oxidative wear. The worn surface of S2 was shown in Figure 5c. It is noted that the typical furrows of abrasive wear were observed and the

worn surface of S2 was smoother than S1. The EDS analysis indicated that the worn surface was highly enriched in Fe, V, Cr and Si, with little O element detected. Therefore, the mechanism of S2 was mainly composed of abrasive wear and adhesive wear. The wear mechanism of S3 was similar to the S2, except that the width and depth of the ploughed furrow decreased as shown in Figure 5d. The main reason for having extremely strong contrast existing among them was the contribution of high hardness and different microstructure characteristics caused by various grain sizes [35]. The previous study demonstrated that strain mainly concentrates close to the grain boundaries; therefore, a material with a larger grain size cracked more easily than those with fewer grain boundaries [42], which meant that the grains with small size can prevent cracking. In addition, the high hardness can resist the ploughing of abrasive grains spalled off from the worn surfaces.



**Figure 5.** SEM morphologies of worn scar on laser cladded Fe-based coatings: (a) worn scar on S1; (b) crack and EDS analysis on S1; (c) worn scar on S2; (d) worn scar on S3.

Figure 6 shows the friction coefficient curves of the laser cladded Fe-based coatings (Figure 6a) and typical cross-sectional profiles of the wear tracks (Figure 6b). It can be seen from Figure 6a that the friction coefficient curve of S1 was similar with the S2. The friction coefficient of S3 was the lowest one. The average friction coefficient of S1, S2 and S3 was 0.707, 0.763 and 0.434, respectively. Figure 6b displays the typical cross-sectional profiles. It was found that the wear resistance of laser cladded coatings was effectively improved with the addition of  $\text{Cr}_3\text{C}_2$  and  $\text{FeV}_{50}$ , based on the significant reduction of the wear depth and the width of the tested samples. The profile of S3 was much smoother than that of S1 and S2, which was consistent with the results of specific wear rate and worn morphologies. In addition, the oxide wear debris played a vital role on affecting the wear resistance. The deepest and widest worn scar indicated that the wear debris generated during reciprocating wear on S1 were maximum, which harm the worn surfaces when the mechanism was abrasive [43]. These observations revealed that S3 possessed the highest wear resistance among the tested samples. The improvement of the wear resistance might mainly be attributed to the effect of grain boundary strengthening, which was improved by the decrease of the grain size, leading to the increase of hardness and preventing the wear debris penetrating into the worn surface.



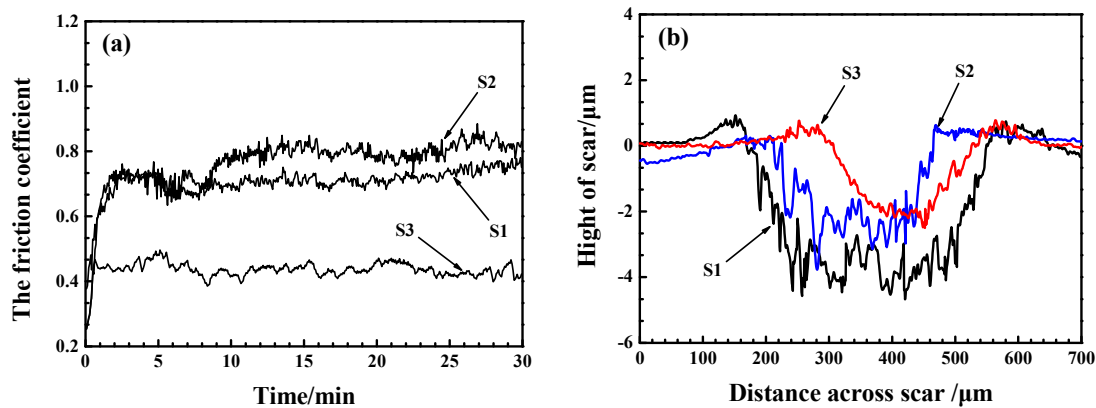


**Figure 6.** The friction coefficient curves of the laser cladded Fe-based coatings (a) and typical cross-sectional profiles of the wear tracks (b).

#### 4. Conclusions

Crack-free Fe-based coatings with high V and Cr content were successfully formed on 35CrMo steel by laser cladding, with a good metallurgical bonding between the coating and the substrate. The coatings of S1 and S2 exhibited single  $\alpha$ -Fe solid solution, while  $\gamma$ -Fe and  $V_8C_7$  were achieved in S3 besides  $\alpha$ -Fe solid solution. The hardness of S1, S2 and S3 was  $62.9 \pm 0.6$  HRC,  $65.3 \pm 0.5$  HRC and  $66.1 \pm 0.6$  HRC, respectively. The corresponding wear resistance of the coatings was proportional to the alloy hardness. The wear resistance of S2 and S3 was 1.7 and 3 times than that of S1. The enhancement in wear resistance of the coating was due to the effect of grain boundary strengthening and solid solution strengthening.

**Acknowledgments:** The authors gratefully acknowledge to the financial support for this research from National Key Research and Development Program of China (No. 2016YFB1100204) and Key Research Project from Science and Technology Commission of Liaoning Province (No. 2017106036) Shenyang Science and Technology Funded Project (Nos. Z18-5-012, 17-29-2-00, Y17-1-031, Z17-2-002).

**Author Contributions:** Haiyang Wang performed the experiments and wrote the manuscript; Song Zhang designed the experimental process; Jingbo Zhang analyzed the data; Chenliang Wu assisted in SEM analysis; Adil O. Abdullah assisted in paper review; and Chunhua Zhang guided the direction of the research.

**Conflicts of Interest:** The authors declare no conflict of interest.

#### References

1. Dobrenizk, L.; Tremmel, S.; Wartzack, S.; Hoffmann, D.C.; Brögelmann, T.; Bobzin, K.; Bagcivan, N.; Musayev, Y.; Hosenfeldt, T. Efficiency improvement in automobile bucket tappet/camshaft contacts by DLC coatings—Influence of engine oil, temperature and camshaft speed. *Surf. Coat. Technol.* **2016**, *308*, 360–373. [[CrossRef](#)]
2. Bayrakceken, H.; Uzun, I.; Tasgetiren, S. Fracture analysis of a camshaft made from nodular cast iron. *Eng. Fail. Anal.* **2006**, *13*, 1240–1245. [[CrossRef](#)]
3. Zhang, C.H.; Wu, C.L.; Zhang, S.; Jia, Y.F.; Guan, M.; Tan, J.Z.; Lin, B. Laser cladding of NiCrSiB on Monel 400 to enhance cavitation erosion and corrosion resistance. *Rare Met.* **2016**, *35*, 1–9. [[CrossRef](#)]
4. He, Y.Z.; Zhang, J.L.; Zhang, H.; Song, G.S. Effects of different levels of boron on microstructure and hardness of  $CoCrFeNiAl_xCu_{0.7}Si_{0.1}B_y$  high-entropy alloy coatings by laser cladding. *Coatings* **2017**, *7*, 7. [[CrossRef](#)]
5. Damm, D.D.; Contin, A.; Barbieri, F.C.; Trava-Airoldi, V.J.; Barquete, D.M.; Corat, E.J. Interlayers applied to CVD diamond deposition on steel substrate: A review. *Coatings* **2017**, *7*, 141. [[CrossRef](#)]
6. He, B.; Zhang, N.N.; Lin, D.Y.; Zhang, Y.; Dong, F.Y.; Li, D.Y. The phase evolution and property of  $FeCoCrNiAlTi_x$  high-entropy alloying coatings on Q235 via laser cladding. *Coatings* **2017**, *7*, 157. [[CrossRef](#)]

7. Fang, L.Y.; Yan, H.; Yao, Y.S.; Zhang, P.L.; Gao, Q.S.; Yang, Q. Reactive fabrication and effect of NbC on microstructure and tribological properties of CrS Co-based self-lubricating coatings by laser cladding. *Materials* **2018**, *11*, 44. [[CrossRef](#)] [[PubMed](#)]
8. Wang, K.M.; Chang, B.H.; Lei, Y.P.; Fu, H.G.; Lin, Y.H. Effect of cobalt on microstructure and wear resistance of Ni-based alloy coating fabricated by laser cladding. *Metals* **2017**, *7*, 551. [[CrossRef](#)]
9. Biswas, S.; Alavi, S.H.; Harimkar, S.P. Effect of laser remelting and simultaneous application of ultrasonic vibrations during laser melting on the microstructural and tribological properties of laser clad Al-SiC composites. *J. Compos. Sci.* **2017**, *1*, 13. [[CrossRef](#)]
10. Zhuang, Q.Q.; Zhang, P.L.; Li, M.C.; Yan, H.; Yu, Z.S.; Lu, Q.H. Microstructure, wear resistance and oxidation behavior of Ni-Ti-Si coatings fabricated on Ti6Al4V by laser cladding. *Materials* **2017**, *10*, 1248. [[CrossRef](#)] [[PubMed](#)]
11. Wang, K.M.; Chang, B.H.; Chen, J.S.; Fu, H.G.; Lin, Y.H.; Lei, Y.P. Effect of molybdenum on the microstructures and properties of stainless steel coatings by laser cladding. *Appl. Sci.* **2017**, *7*, 1065. [[CrossRef](#)]
12. Zhang, L.; Wang, C.S.; Qian, S.N.; Yu, Q.; Chuang, Q. Microstructure and wear resistance of laser-clad (Co, Ni)<sub>61.2</sub>B<sub>26.2</sub>Si<sub>7.8</sub>Ta<sub>4.8</sub> coatings. *Metals* **2017**, *7*, 419. [[CrossRef](#)]
13. Chen, Y.X.; Guo, Y.B.; Lu, B.F.; Xu, M.J.; Xu, J.H. Microstructure and properties of the interface area in the laser clad Ni based coatings on the 1Cr10Mo1NiWVNbN steel. *Metals* **2017**, *7*, 175. [[CrossRef](#)]
14. Zhang, C.H.; Zhang, H.; Wu, C.L.; Zhang, S.; Sun, Z.L. Multi-layer functional graded stainless steel fabricated by laser melting deposition. *Vacuum* **2017**, *141*, 181–187. [[CrossRef](#)]
15. Yao, H.H.; Zhou, Z.; Wang, L.; Tan, Z.; He, D.Y.; Zhao, L.D. Thermal conductivity and wear behavior of HVOF-sprayed Fe-based amorphous coatings. *Coatings* **2017**, *7*, 173. [[CrossRef](#)]
16. Rogachev, S.O.; Sundeev, R.V.; Khatkevich, V.M. Evolution of the structure and strength of steel/vanadium alloy/steel hybrid material during severe plastic deformation. *Mater. Lett.* **2016**, *173*, 123–126. [[CrossRef](#)]
17. Li, Y.S.; Zhu, L.H.; Liu, C.W.; Shi, S.J. Nanoscale phase evolution during continuum decomposition of Fe-Cr alloys. *Materials* **2017**, *10*, 1431. [[CrossRef](#)] [[PubMed](#)]
18. Huang, C.A.; Chen, J.Y.; Wang, H.; Lai, P.L. Anneal-hardening behavior of Cr-Fe-C alloy deposits prepared in a Cr<sup>3+</sup>-based bath with Fe<sup>2+</sup> ions. *Materials* **2017**, *10*, 1392. [[CrossRef](#)] [[PubMed](#)]
19. Boucher, R.; Berger, O.; Leyens, C. Magnetic properties of bulk and thin film Cr-Al-C compounds. *Surf. Eng.* **2016**, *32*, 172–177. [[CrossRef](#)]
20. Caiazzo, F.C.; Sisti, V.; Trasatti, S.P.; Trasatti, S. Electrochemical characterization of multilayer Cr/CrN-based coatings. *Coatings* **2014**, *4*, 508–526. [[CrossRef](#)]
21. Bhatti, J.; Fazal, M.A.; Bushroa, A.R.; Khan, A.F.; Quazi, M.M. Structural and mechanical properties of (Cr, Ni) N single and gradient layer coatings deposited on mild steel by magnetron sputtering. *Mater. Charact.* **2013**, *78*, 69–78. [[CrossRef](#)]
22. Yu, L.H.; Luo, H.; Bian, J.G.; Ju, H.B.; Xu, J.H. Research on microstructure, mechanical and tribological properties of Cr-Ti-B-N films. *Coatings* **2017**, *7*, 137.
23. Ke, D.; Pan, Y.; Xu, Y.; Yang, L.; Wu, R.; Lu, Z. Microstructure and mechanical properties of Mo<sub>2</sub>FeB<sub>2</sub> ceramic-steels with Nb/V addition. *Adv. Appl. Ceram.* **2017**, *116*, 92–98. [[CrossRef](#)]
24. Kawalec, M.; Górný, M. Influence of carbides morphology on the mechanical properties for Fe-C-V alloys. *Int. J. Cast Met. Res.* **2016**, *29*, 34–39. [[CrossRef](#)]
25. Gwon, H.; Kim, J.K.; Shin, S.; Cho, L.; Cooman, B.C.D. The effect of vanadium micro-alloying on the microstructure and the tensile behavior of TWIP steel. *Mater. Sci. Eng. A* **2017**, *696*, 416–428. [[CrossRef](#)]
26. Gao, W.Y.; Zhang, Z.Y.; Zhao, S.S.; Wang, Y.B.; Chen, H.; Lin, X.C. Effect of a small addition of Ti on the Fe-based coating by laser cladding. *Surf. Coat. Technol.* **2016**, *291*, 423–429. [[CrossRef](#)]
27. Pryds, N.H.; Juhl, T.W.; Pedersen, A.S. The solidification characteristics of laser surface-remelted Fe-12Cr-nC alloys. *Metall. Mater. Trans. A* **1999**, *30*, 1817–1826. [[CrossRef](#)]
28. Chang, G.W. *Crystal Growth and Control during Solidification of Metal*; Metallurgical Industry Press: Beijing, China, 2002. (In Chinese)
29. Hunt, J.D. Steady state columnar and equiaxed growth of dendrites and eutectic. *Mater. Sci. Eng.* **1984**, *65*, 75–83. [[CrossRef](#)]
30. Yogo, Y.; Tanaka, K.; Ikehata, H.; Iwata, N.; Nakanishi, K.; Ishikawa, T. Calculation for grain growth rate of carbon steels by solute drag model considering segregation effect of each substitutional element. *Mater. Sci. Technol.* **2011**, *27*, 1593–1598. [[CrossRef](#)]

31. Parameswaran, P.; Saroja, S.; Vijavalakshmi, M.; Raghunathan, V.R. Decomposition modes of austenite in Cr Mo ferritic steels. *J. Nucl. Mater.* **1996**, *232*, 226–232. [[CrossRef](#)]
32. Tuominen, J.; Naekki, J.; Pajukoski, H.; Hyvärinen, L.; Vuoristo, P. Microstructural and abrasion wear characteristics of laser-clad tool steel coatings. *Surf. Eng.* **2016**, *32*, 923–933. [[CrossRef](#)]
33. Chen, C.J.; Wang, M.C.; Wang, D.S.; Jin, R.; Liu, Y.M. Laser cladding of Mg20Al80 powder on ZM5 magnesium alloy. *Corros. Eng. Sci. Technol.* **2013**, *42*, 130–136. [[CrossRef](#)]
34. Ghasemi, R.; Elmquist, L.; Svensson, H.; König, M.; Jarfors, A.E.W. Mechanical properties of solid solution strengthened CGI. *Int. J. Cast Met. Res.* **2016**, *29*, 98–105. [[CrossRef](#)]
35. Sharma, A.; Kumar, S.; Singh, G.; Pandey, O.P. Effect of particle size on wear behavior of Al–garnet composites. *Part. Sci. Technol.* **2015**, *33*, 234–239. [[CrossRef](#)]
36. Jian, S.R.; Chen, G.J.; Hsu, W.M. Mechanical properties of Cu<sub>2</sub>O thin films by nanoindentation. *Materials* **2013**, *6*, 4505–4513. [[CrossRef](#)] [[PubMed](#)]
37. Singh, K.K.; Sangal, S.; Murty, G.S. Hall–Petch behaviour of 316L austenitic stainless steel at room temperature. *Mater. Sci. Technol.* **2002**, *18*, 165–172. [[CrossRef](#)]
38. Morozova, A.; Kaibyshev, R. Grain refinement and strengthening of a Cu–0.1Cr–0.06Zr alloy subjected to equal channel angular pressing. *Philos. Mag. A* **2017**, *97*, 2053–2076. [[CrossRef](#)]
39. Wu, C.L.; Zhang, S.; Zhang, C.H.; Zhang, H.; Dong, S.Y. Phase evolution and properties in laser surface alloying of FeCoCrAlCuNi high-entropy alloy on copper substrate. *Surf. Coat. Technol.* **2017**, *315*, 368–376. [[CrossRef](#)]
40. Algodí, S.J.; Murray, J.W.; Brown, P.D.; Clare, A.T. Wear performance of TiC/Fe cermet electrical discharge coatings. *Wear* **2018**, *402–403*, 109–123. [[CrossRef](#)]
41. Wang, B.; Yao, B.; Han, Z. Annealing effect on wear resistance of nanostructured 316L stainless steel subjected to dynamic plastic deformation. *J. Mater. Sci. Technol.* **2012**, *28*, 871–877. [[CrossRef](#)]
42. Wang, Z.H.; Sun, S.H.; Wang, B.; Shi, Z.; Fu, W. Importance and role of grain size in free surface cracking prediction of heavy forgings. *Mater. Sci. Eng. A* **2015**, *625*, 321–330. [[CrossRef](#)]
43. Varenberg, M.; Halperin, G.; Etsion, I. Different aspects of the role of wear debris in fretting wear. *Wear* **2002**, *252*, 902–910. [[CrossRef](#)]



© 2018 by the authors. Licensee MDPI, Basel, Switzerland. This article is an open access article distributed under the terms and conditions of the Creative Commons Attribution (CC BY) license (<http://creativecommons.org/licenses/by/4.0/>).